Study on Weldability and Mechanical Properties of RSW Annular-Nugget Joint: Part 2 — Mechanical Properties Characterization

Critical factors influencing the peak tensile-shear load under interfacial fracture and pullout fracture modes were identified

BY S. WANG, G. XU, J. DONG, Y. QIU, Q. FAN, Z. HUANG, AND X. GU

Abstract

The mechanical properties of DP780 steel welded using resistance spot welding (RSW) were evaluated by comparing a new ring conductive electrode (RSW-R) with a spherical electrode (RSW-S). Part 1 of this study demonstrated that RSW-R optimizes heat distribution and current density, significantly broadening the weldability range of DP780 steel. Building on this foundation, the present study further investigated the impact of RSW-R on mechanical properties. Compared to RSW-S, RSW-R increased the upper limit of peak tensile-shear loads by 15.9% and failure energy by 91.5%. Moreover, at similar peak tensile-shear loads (11 kA for RSW-S, 10 kA for RSW-R), RSW-R reduced joule heat input by 26.8% and surface indentation by 87.3% compared to RSW-S. The peak tensile-shear load was found to be related to the nugget area when interfacial fracture occurred, while nugget diameter played a more significant role in pullout fracture (PF) mode. Notably, in PF mode, the unconnected region at the inner diameter did not substantially compromise the tensile-shear mechanical properties. Electrode life tests further confirmed that RSW-R achieved stable joint formation for up to 140 consecutive welds, demonstrating durability comparable to RSW-S.

https://doi.org/10.29391/2025.104.030

Keywords

- Resistance Spot Welding
- DP780 Steel
- Annular-Nugget
- Tensile-Shear Test
- Failure Mode
- Mechanical Properties

Introduction

Resistance spot welding (RSW) is one of the most widely used welding techniques in automobile manufacturing (Refs. 1–3). In modern vehicles, spot welds typically range from 2000 to 5000 per vehicle (Ref. 4). These welds are crucial for efficiently transferring loads and absorbing impact energy during collisions, making the quality of the weld joints vital to vehicle safety design (Ref. 5).

Advanced high strength steels (AHSSs) are extensively used in automotive manufacturing to reduce weight, improve fuel efficiency, and enhance mechanical performance (Ref. 6). Despite their favorable strength and ductility, AHSS weld joints can contain brittle martensitic microstructures, which form due to the rapid cooling of the weld nugget at rates ranging from 1000°C/s to 10,000°C/s (Ref. 7). These microstructural characteristics reduce the fracture toughness of the joints. Compared to low-carbon steel, AHSS RSW joints are more susceptible to interfacial fracture, with crack propagation occurring through the nugget (Ref. 8).

Several researchers have investigated various methods to address these challenges. Soomro et al. explored the effect of post-weld heat treatment on the load-bearing capacity and failure energy of dual-phase steels. Their findings demonstrated that the treatment increased the extent of tempered martensite, thereby significantly enhancing

Table 1 — Welding Parameters of the Welding Process

Electrode	Squeezing Time	Welding Time	Holding Time	Electrode Force	Welding Current
RSW-S	200 ms	200 ms	400 ms	4 kN	7, 8, 9, 10, 11, 12 kA
RSW-R	200 ms	200 ms	400 ms	4 kN	8, 9, 10, 11, 12, 13 kA
RSW-S	200 ms	200, 333, 466, 600 ms	400 ms	4 kN	8 kA
RSW-R	200 ms	200, 300, 400 ms	400 ms	4 kN	9.5 kA

both fracture toughness and peak failure energy (Refs. 9, 10). Ambriz and Ren et al. applied cold-working treatments before and after welding, effectively improving the fatigue strength of RSW joints by optimizing residual stress distribution (Refs. 11, 12). Li et al. (Ref. 13) improved the strength of medium-manganese TRIP steel joints by incorporating shims to produce larger nuggets. Additionally, Li et al. refined the grain structure in the nugget by applying a magnetic field, which reduced grain orientation. The external magnetic force induced eccentric movement in the molten metal, altering the nugget dimensions and enhancing the quality of RSW joints in austenitic stainless steel (Ref. 14). These studies have significantly advanced the mechanical properties of RSW joints. However, as pointed out by Pouranvari et al. (Ref. 15), while such methods can enhance joint properties, they may also lead to considerable increases in welding time and reductions in production efficiency.

Some researchers have enhanced mechanical properties while maintaining productivity by modifying electrode designs. Deng et al. developed a multi-ring dome electrode that improved current distribution by disrupting the oxide layer on the sheet's surface, resulting in larger nuggets and stronger microstructures (Ref. 16). Chen et al. introduced a micro-concave electrode that optimized current density distribution, significantly enhancing the tensile-shear performance of Q&P steel RSW joints (Ref. 17). Kim et al. designed deep hollow electrodes for welding three-sheet AHSS, which reduced expulsion and broadened the welding current range (Ref. 18). Ren et al. embedded insulating ceramics into the electrodes to improve current distribution, producing large-diameter nuggets and joints with superior mechanical properties (Refs. 19–21). However, these electrode modifications may introduce grooves or protrusions on the joint surface, potentially compromising surface quality and causing stress concentration, which could reduce the mechanical properties. Additionally, the differences in thermal physical properties between ceramic insulation cores and copper alloy electrodes may negatively impact heat dissipation efficiency and electrode life.

Building on previous research, a new ring conductive electrode (RSW-R) was developed in this study to enhance the mechanical properties of RSW joints in DP780 steel. The new electrode modifies the current distribution of the conventional F-type electrode (RSW-S) while maintaining production efficiency. In the first part of this study (Ref. 22), the weldability of DP780 steel was analyzed by comparing RSW-R and RSW-S in terms of joint current density and thermal field distribution. The growth mechanism of the annular-nugget was also examined. The results demonstrated that the annular current distribution of RSW-R reduced the current density at the faying surface, lowered total joule heat input and generation rate, and significantly expanded the weldability range of DP780 steel. This annular current distribution not only shifted the initiation point for annular-nugget growth but also enabled a larger nugget diameter by increasing the upper limit of the welding current. Additionally, RSW-R minimized surface indentation depth.

The second part of the study focused on comparing the peak tensile-shear load and failure energy of DP780 steel welded with both electrode types. Additionally, variations in nugget dimensions with increasing weld counts were evaluated, and the approximate life of both electrodes, without dressing, was estimated. Building on the annular-nugget growth mechanism discussed in the first part, further exploration of the relationship between current density distribution, nugget dimensions, and mechanical properties was conducted.

Experimental Details

Material and Welding Process

DP780 steel samples (105 × 45 × 1.2 mm) were welded using a novel setup, the details of which, including the preparation of the conductive ring electrode, were provided in Part 1 (Ref. 22). The welding parameters, including welding current, electrode force, and welding time, are summarized in Table 1. Welding currents were chosen for the electrode life tests to produce comparable mechanical properties in tensile-shear tests (10 kA for RSW-R and 11 kA for RSW-S). Critical dimensions—such as the inner and outer diameters, penetration, and length of the heat-affected zone (HAZ)—were measured at four intervals over 220 consecutively welded joints. These intervals included specimens numbered 1–10, 71–80, 141–150, and 211–220, with ten samples per interval to minimize the influence of random variations in the experimental process. The welding cooling water flow rate was maintained at 6 L/min, and the off-time was set to at least 1 min.

Electrode surface degradation was evaluated using carbon imprints, with deterioration characterized by changes in the contact area between the upper and lower electrodes under constant force. Due to significant shape differences between

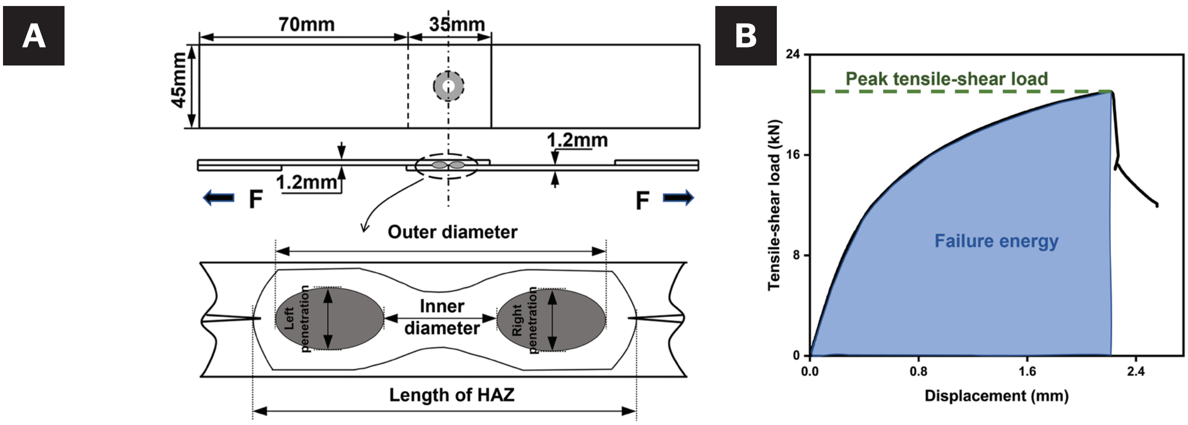

Fig. 1 — A — Dimensions of specimen and characterization of joint areas; B — schematic diagram of tensile-shear mechanical properties.

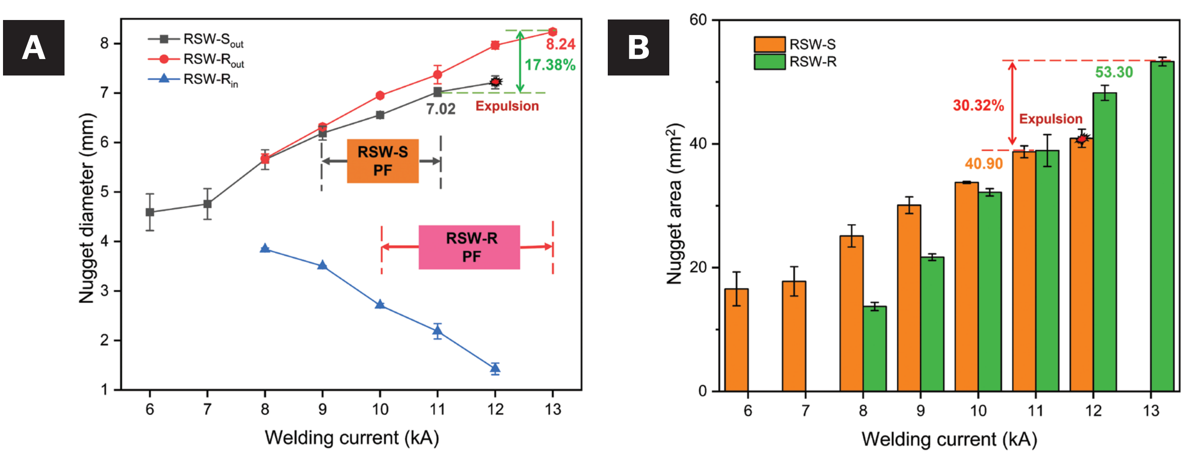

Fig. 2 (from Part 1) — The variation of nugget size with welding current under RSW-R and RSW-S conditions: A — The inner and outer diameters of nuggets with welding current; B — the nugget area with welding current.

annular and elliptical nuggets, the degree of electrode degradation was assessed by comparing the relative change rate in nugget dimensions. Nugget dimensions from the first interval served as the baseline, and subsequent intervals were compared accordingly.

Mechanical Test and Metallographic Observation

Welded specimens were subjected to uniaxial tensile-shear testing using an MTS810 machine to evaluate the mechanical properties of RSW joints. The specimen dimensions followed ANSI/AWS/SAE/D8.9, *Recommended Practices for Test Methods for Evaluating the Resistance Spot Welding Behavior of Automotive Sheet Steel Materials* (Ref. 23). To minimize bending moments during testing, DP780 shims (45 × 45 × 1.2 mm) were placed between the specimen and the hydraulic grips, as illustrated in Fig. 1A. The crosshead speed was set at 2.0 mm/min. Mechanical test results were recorded as peak tensile-shear load and failure energy, with failure energy calculated based on prior studies (Refs. 10, 24, 25) and represented by the blue area in Fig. 1B. At least three sets of welded samples were used for each welding parameter to evaluate mechanical properties and nugget dimensions. Under RSW-S conditions, when the welding current was 12 kA, only one set of samples was welded for mechanical property testing due to the expulsion.

For metallographic analysis, RSW joints were sectioned through the center using wire-cut electrical discharge machining. The samples were polished following standard protocols and then etched with a 2% Nital solution (Ref. 26). Optical imaging was conducted using a ZEISS Scope A1 digital microscope. The detailed microstructural observations of each subregion were performed with a TESCAN-VEGA3 XMU scanning electron microscope at an accelerating voltage of 20 kV. The characterization of each joint region is shown in Fig. 1A.

Results

Nugget Dimensions

Figure 2 illustrates the variations in inner diameter, outer diameter, and nugget area of RSW-S and RSW-R joints as a

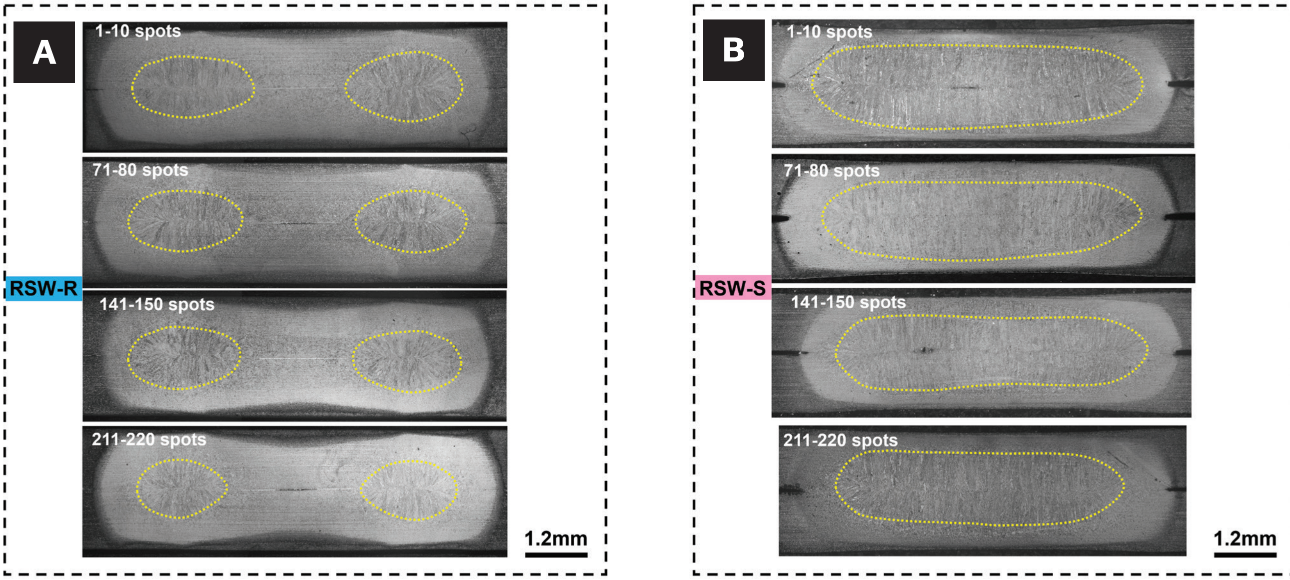

Fig. 3 — The cross-sectional metallographic images of the joints for both electrode conditions as the number of welds increased: A — Under RSW-R conditions; B — under RSW-S conditions.

function of welding current under identical welding time. The outer diameter of RSW-R joints consistently exceeded that of RSW-S joints for the same welding parameters. Additionally, the nugget area and the difference in outer diameters between RSW-R and RSW-S joints increased with the welding current, while the inner nugget diameter decreased. The peak nugget area of RSW-R joints was 30.32% larger than RSW-S joints.

Figures 3A and B present the cross-sectional metallographic images of the joints for both electrode conditions as the number of welds increased. The nugget dimensions for both electrodes remained relatively stable through the first 150 welds compared to the initial interval (1–10 welds). However, in the fourth interval (211–220 welds), a significant increase in the inner diameter of the annular-nugget was observed, and the diameter of the elliptical nugget notably decreased, resulting in a marked reduction in the volume of both nugget types. Detailed information on nugget dimensions across the four intervals for both electrode conditions is provided in Fig. 4. Specifically, Figs. 4A and C show the average nugget dimensions for each interval (with a sample size of ten per interval) under both electrode conditions. Figures 4B and D illustrate the relative changes in the average nugget dimensions for the latter three intervals compared to the first.

From Figs. 4A and B, it can be observed that aside from the penetration depth, the inner diameter, outer diameter, length of the HAZ, and nugget area of the annular-nugget all showed varying degrees of increase compared to the first interval. Notably, the inner diameter of the annular-nugget experienced a significant rise in the fourth interval (+26.0%). At the same time, the relative change rate of the nugget area gradually diminished with the number of welds. In contrast, Figs. 4C and D show that under spherical electrode conditions, the overall trend of nugget dimensions decreased gradually as the number of welds increased. The nugget diameter in the third interval decreased by 10.9% compared to the first interval, while the nugget bonding area in the third interval decreased by 20.5% compared to the first interval. Furthermore, Figs. 4A and C reveal that the carbon imprint area increased with the number of welds for both electrode types.

Mechanical Behavior and Fracture Mode Characterization

Figure 5 illustrates the variations in peak tensile-shear load and failure energy as a function of welding current for DP780 steel RSW joints under identical welding times but with different electrode conditions. The pink-shaded region represents the current range for pullout fracture under RSW-S conditions, and the blue-shaded region corresponds to the current range for pullout fracture under RSW-R conditions. RSW-R significantly enhanced the peak tensile-shear load by approximately 15.9% (+3.24 kN) and increased the upper limit of failure energy by around 91.5% (+31.48 J). Expulsion negatively impacted both the peak tensile-shear load and failure energy. Under RSW-S conditions, the tensile-shear load and failure energy initially increased with the welding current but decreased once expulsion occurred. In contrast, under RSW-R conditions, the tensile-shear load consistently increased with the welding current, while failure energy experienced a significant drop at a welding current of 13 kA.

According to AWS D8.2M, *Specification for Automotive Weld Quality—Resistance Spot Welding of Aluminum* (Ref. 27), eight fracture modes are recognized in RSW, with interfacial fracture (IF) and pullout fracture (PF) observed in this study.

It is worth noting that although the IF mode typically exhibits lower failure energy and peak tensile-shear load, this does not imply that it is unacceptable for engineering applications. On the contrary, when the fused area is sufficiently large, joints failing in the IF mode can still meet practical requirements. In this study, the PF mode demonstrated superior

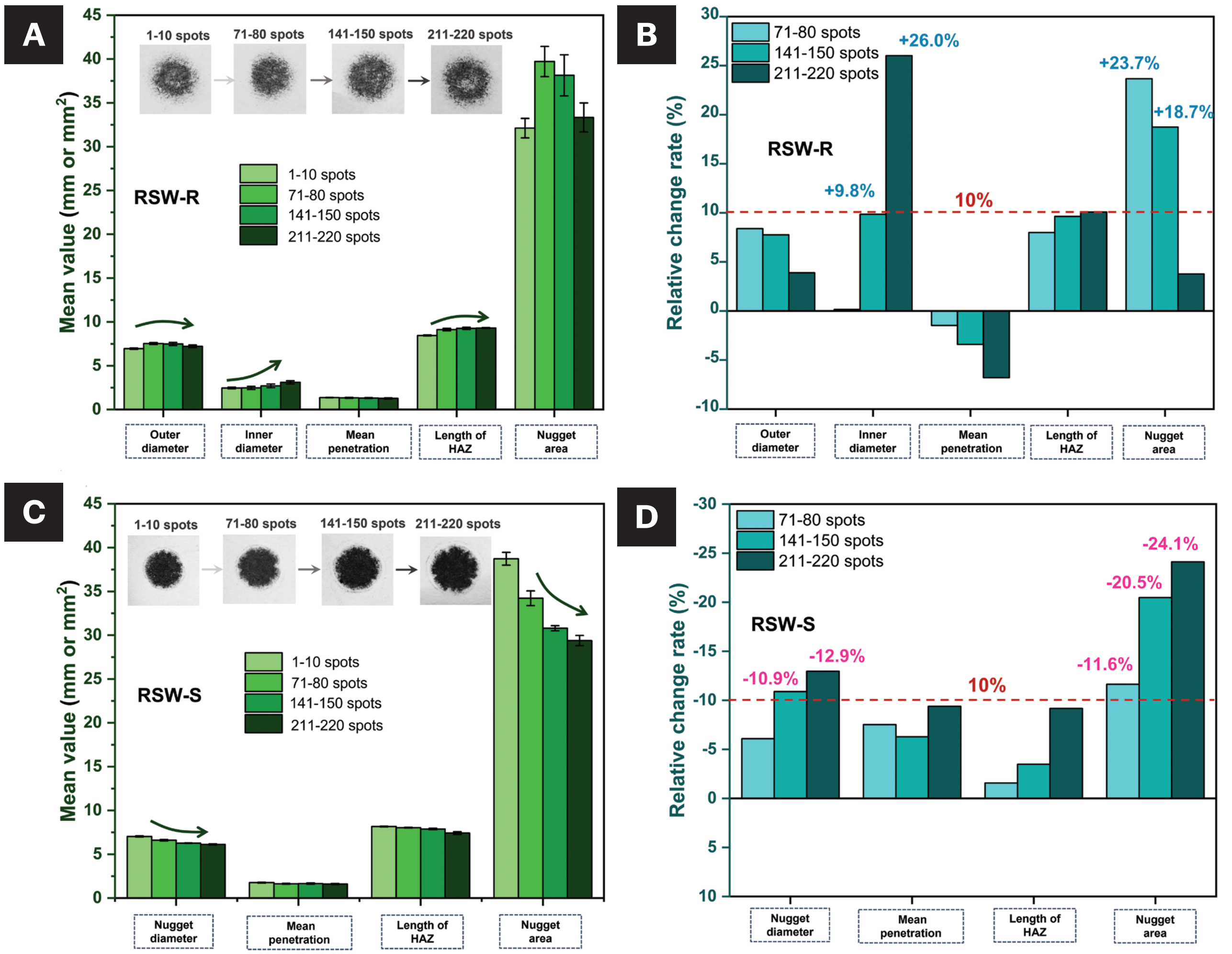

Fig. 4 — The variation of nugget size (the inner diameter, outer diameter, penetration, the length of HAZ, and nugget area) with the number of welds under two different electrode conditions: A — Diagram of the nugget's average dimensions in four intervals under RSW-R conditions; B — relative change rate of nugget dimensions in the latter three intervals compared to the initial interval under RSW-R conditions; C — diagram of the nugget's average dimensions in four intervals under RSW-S conditions; D — relative change rate of nugget dimensions in the latter three intervals compared to the initial interval under RSW-S conditions.

mechanical performance; therefore, PF mode joints were primarily regarded as indicators of high joint quality in the present evaluation.

Figures 6 and 7 illustrate the typical fracture characteristics at different currents for IF (RSW-S: 8 kA, RSW-R: 9 kA). Please note that the lowest magnification images of the fracture surfaces were captured at different magnifications for the RSW-R and RSW-S joints.

As shown in Fig. 6, the edge region of the nugget (Region A) exhibited distinct cleavage steps, indicating a cleavage fracture mode. Region B, in contrast, transitioned into a mixed fracture mode, with cleavage and ductile fractures coexisting. In Region C, uniformly sized shear dimples aligned along the shear direction were observed. Similarly, in Fig. 7A, which depicts the IF surface of the annular-nugget, shear dimples aligned along the shear direction were also observed in the nugget region. The presence of shear dimples showed that the failure mechanism involved shear localization of plastic flow, driven by the shear stress state at the crack tip (Ref.

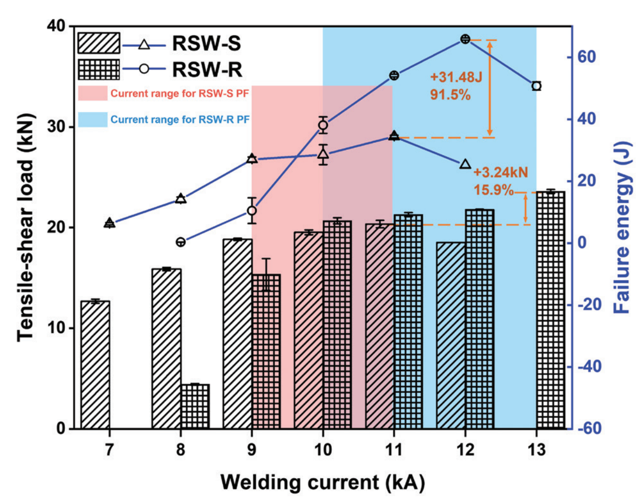

Fig. 5 — Schematic of weldability range for two types of electrode conditions and the variation tensile-shear loading, failure energy with welding current.

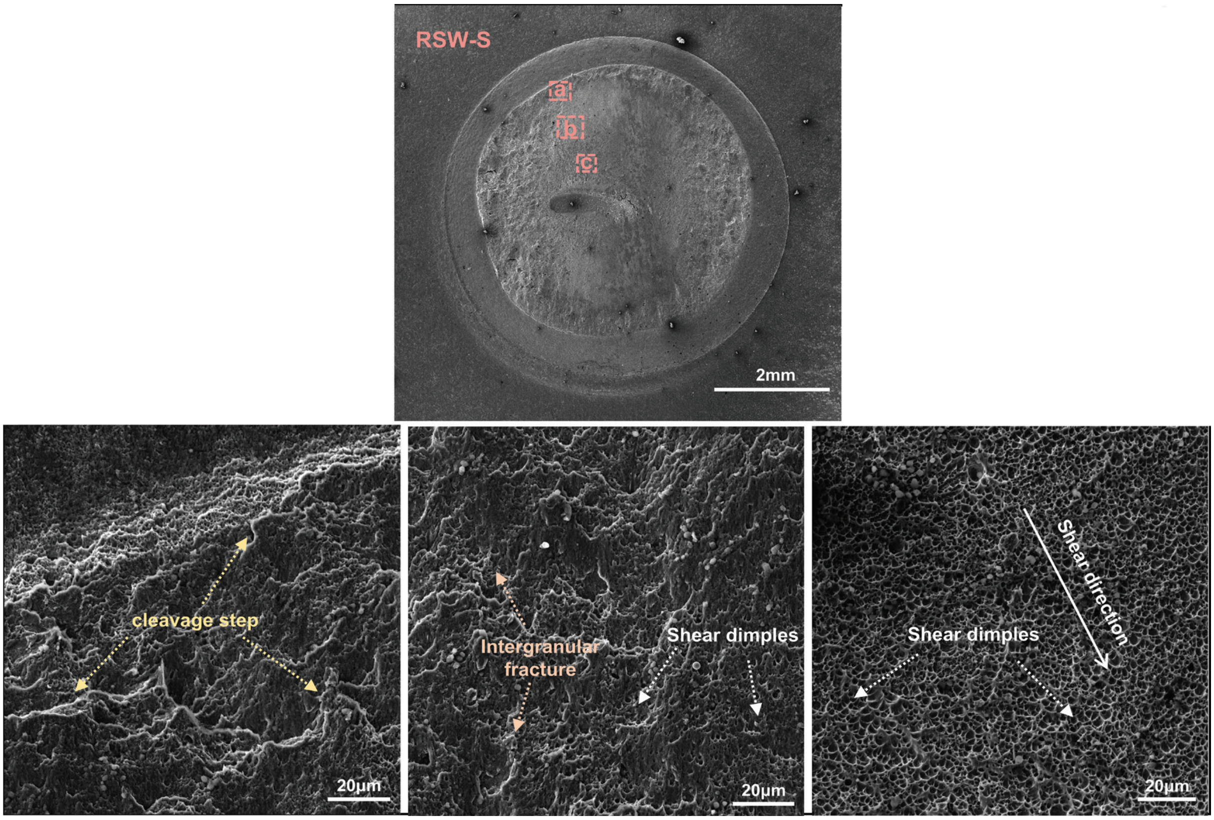

Fig. 6 — Typical SEM images of the IF fracture surfaces of the joints under RSW-S conditions.

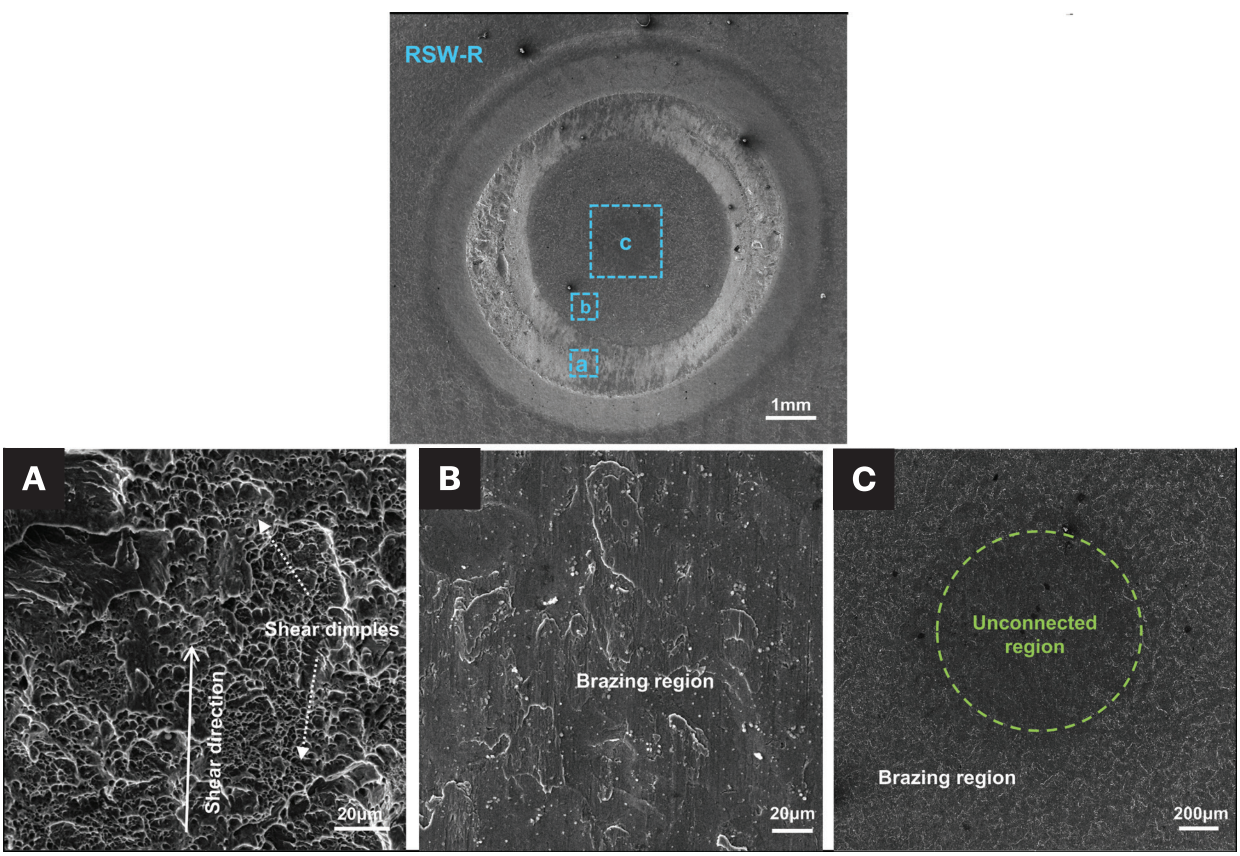

Fig. 7 — Typical SEM images of the IF fracture surfaces of the joints under RSW-R conditions.

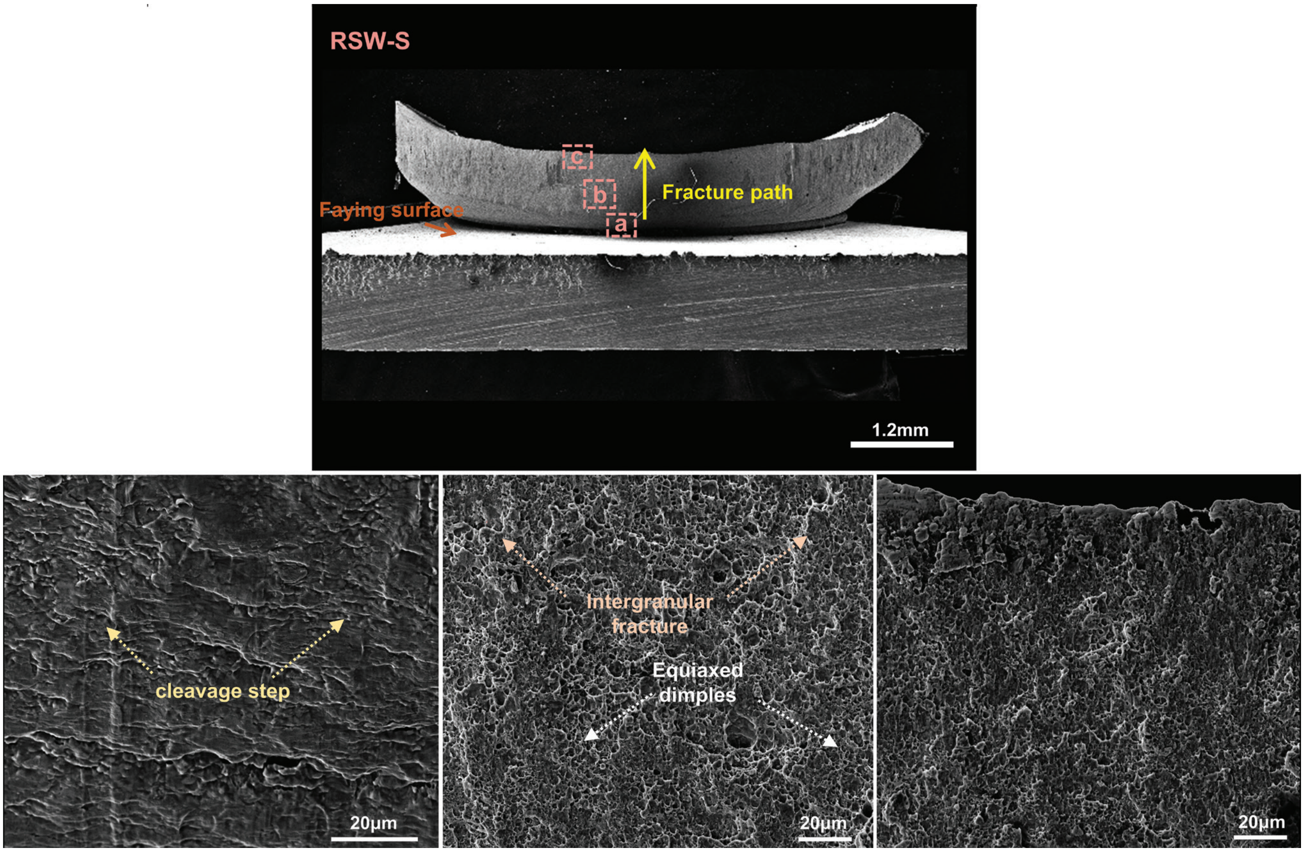

Fig. 8 — Typical SEM images of the PF fracture surfaces of the joints under RSW-S conditions.

28). Unlike the elliptical nugget, the inner diameter region of the annular-nugget (Region B) exhibited characteristics of a brazed interface fracture, while the central region of the joint, shown in Fig. 7C, displayed a circular unconnected region.

Figures 8 and 9 present the typical fracture characteristics for pullout fracture at a welding current of 10 kA under both electrode conditions. The PF fracture surfaces under both conditions displayed similar features: cleavage steps in Region A, indicating a cleavage fracture mode; intergranular fracture characteristics and equiaxed dimples in Region B, suggesting a transition to a mixed fracture mode combining cleavage and ductile fracture; and a pronounced intergranular fracture in Region C, where the number of dimples gradually decreased along the crack propagation direction.

To investigate the factors influencing the peak tensile-shear load of DP780 steel under different fracture modes, the correlations between nugget diameter, nugget area, and peak tensile-shear load for both PF and IF modes were analyzed. As shown in Fig. 10, the correlation coefficient between nugget area and peak tensile-shear load was 0.85 for IF, significantly higher than the correlation between nugget diameter and peak tensile-shear load. Conversely, the correlation coefficient for PF between nugget diameter and peak tensile-shear load was 0.90, considerably higher than that between nugget area and peak tensile-shear load. These results indicated that in IF mode, the nugget area primarily influences the peak tensile-shear load. In contrast, the nugget diameter in PF mode showed a stronger linear correlation with the peak tensile-shear load.

Mechanical Model

This section presents a modified model based on metallurgical factors, building upon the theoretical framework established by previous scholars to determine the factors influencing the mechanical properties of RSW (Refs. 26, 29–31). Figure 11 illustrates a mechanical model with a simplified representation of stress distribution across the nugget, heat-affected zone, and base material under tensile-shear load. The faying surface experienced shear stress, while the HAZ of the outer side of the nugget and the base material experienced tensile stress. According to the failure mode transition criterion proposed by Pouranvari et al. (Refs. 31, 32), interface fracture occurred when the maximum shear force at the faying surface was less than the maximum tensile force in the joint's weakest area. In contrast, pullout fracture occurred when the tensile force exceeded the shear force.

Figure 12A shows the idealized model of the annular-nugget. Figure 12B details the shear stress distribution at the faying surface under the tensile-shear load. This study idealized nugget geometry as an annular drum-shaped structure to better align with practical conditions. Under pure tensile-shear loading, the shear stress at the faying surface varies linearly from the center to the edge of the nugget (Ref. 35).

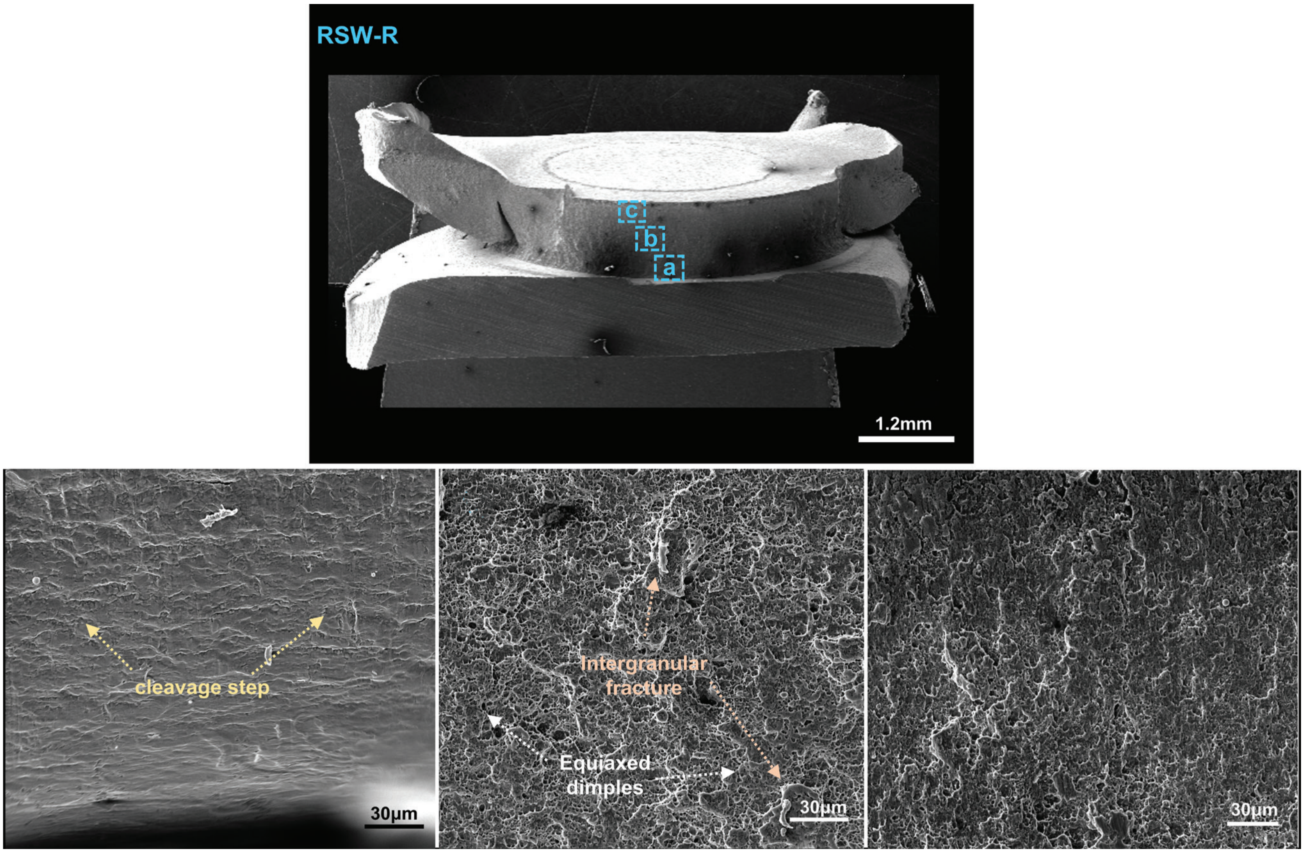

Fig. 9 — Typical SEM images of the PF fracture surfaces of the joints under RSW-R conditions.

The maximum shear force that the faying surface can withstand is:

$$F_{IF} = \int_0^{R_{in}} \frac{x}{R_{out}} \tau_{max} \cdot 2\left(\sqrt{{R_{out}}^2 - x^2} - \sqrt{{R_{in}}^2 - x^2}\right) dx + \int_{R_{in}}^{R_{out}} \frac{x}{R_{out}} \tau_{max} \cdot 2\sqrt{{R_{out}}^2 - x^2} dx = \frac{2\tau_{max}}{R_{out}}\left[\frac{{R_{out}}^3}{3} - \frac{{R_{in}}^3}{3}\right] \quad (1)$$

In the equation, τ_x denotes the shear strength at position x on the faying surface of the nugget while τ_{max} is the maximum tensile-shear stress the nugget can withstand at the point of interface failure.

According to Sun et al. (Ref. 30), the tensile stress around the nugget exhibits a sinusoidal distribution. Figures 12C and D illustrate the detailed tensile stress distribution on the outer side of the nugget when the joint is subjected to tensile-shear loading. The maximum tensile force that the side of the annular-nugget can withstand at the point of pullout fracture is given by:

$$\mathrm{F}_{PF1} = \frac{\sigma_{max1}}{R_{out}} \cdot \int_{-\frac{\pi}{2}}^{\frac{\pi}{2}} cos^2\beta d\beta \cdot \int_0^H \left({R_{out}}^2 - h^2\right) dh = \frac{H\pi\sigma_{max1}}{2}\left(R_{out} - \frac{H^2}{3R_{out}}\right) \quad (2)$$

The maximum tensile force that the base material above the annular nugget can withstand is:

$$F_{PF2} = \sigma_{max2}(T - H) \cdot \left(\sqrt{{R_{out}}^2 - H^2}\right) \cdot 2\int_0^{\frac{\pi}{2}} cos^2\beta' d\beta' = \frac{\pi\sigma_{max2}(T - H) \cdot (\sqrt{{R_{out}}^2 - H^2})}{2} \quad (3)$$

The tensile force required for the pullout fracture of the spot weld joint is:

$$F_{PF} = \begin{cases} F_{PF1} & F_{PF1} \geq F_{PF2} \\ F_{PF2} & F_{PF2} > F_{PF1} \end{cases} \quad (4)$$

According to the Tresca criterion, the material's tensile strength is twice its shear strength, i.e.:

$$\frac{\sigma_{max1}}{\tau_{max}} = \frac{2\sigma_{HAZ}}{\sigma_{FZ}} \; \frac{\sigma_{max2}}{\tau_{max}} = \frac{2\sigma_{BM}}{\sigma_{FZ}} \quad (5)$$

$$\begin{cases} \sigma_{HAZ} = B_1 V_{HAZ} \\ \sigma_{FZ} = B_2 V_{FZ} \\ \sigma_{BM} = B_3 V_{BM} \end{cases} \quad (6)$$

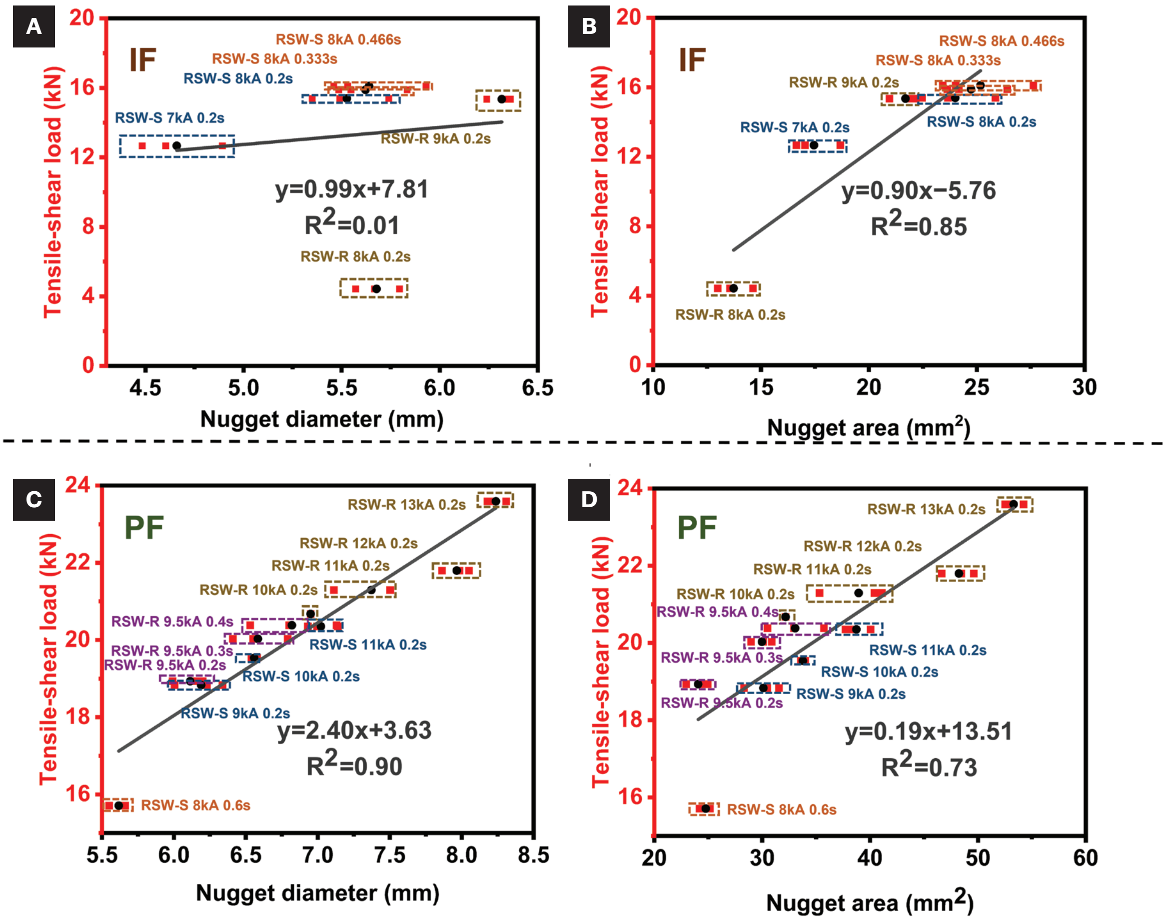

Fig. 10 — Relationship between nugget size and peak tensile-shear load: A — The nugget diameter during IF; B — the nugget area during IF; C — the nugget diameter during PF; D — the nugget area during PF. In the figures, dashed rectangles indicate nuggets produced under identical welding parameters. Red dots within the rectangles represent individual experimental measurements of nugget size, while black dots indicate the corresponding average nugget size. The tensile-shear load value for each group is the average under the given welding parameters. Additionally, the font colors of the welding parameters vary depending on the electrode type, welding current, and welding time.

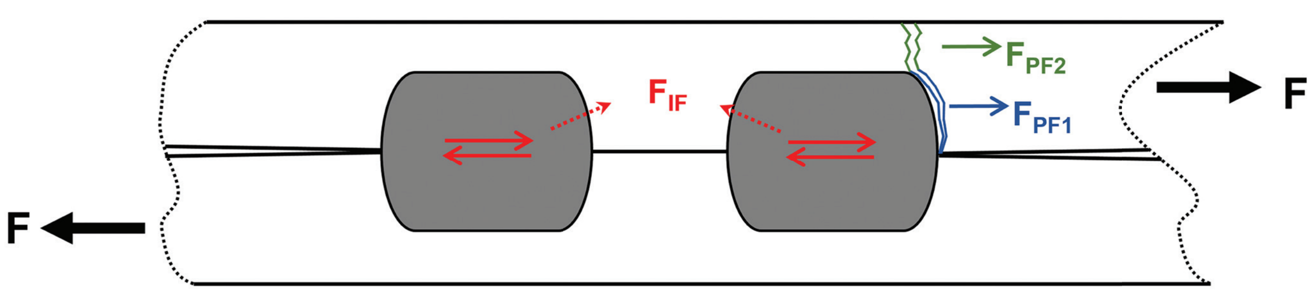

Fig. 11 — A simple model describing stress distribution at the interface and circumference of a weld nugget during the tensile-shear load.

A direct relationship exists between the material's tensile strength and its hardness. By substituting the relevant parameters into the above formulas, the maximum shear force and maximum tensile force that the RSW joint can withstand can be determined.

In the formulas, σ_{max1} is the maximum tensile strength that the side surface of the annular-nugget can withstand during pullout fracture, and σ_{max2} is the maximum tensile strength that the outer base material along the thickness direction of the annular-nugget can withstand during pullout fracture. H

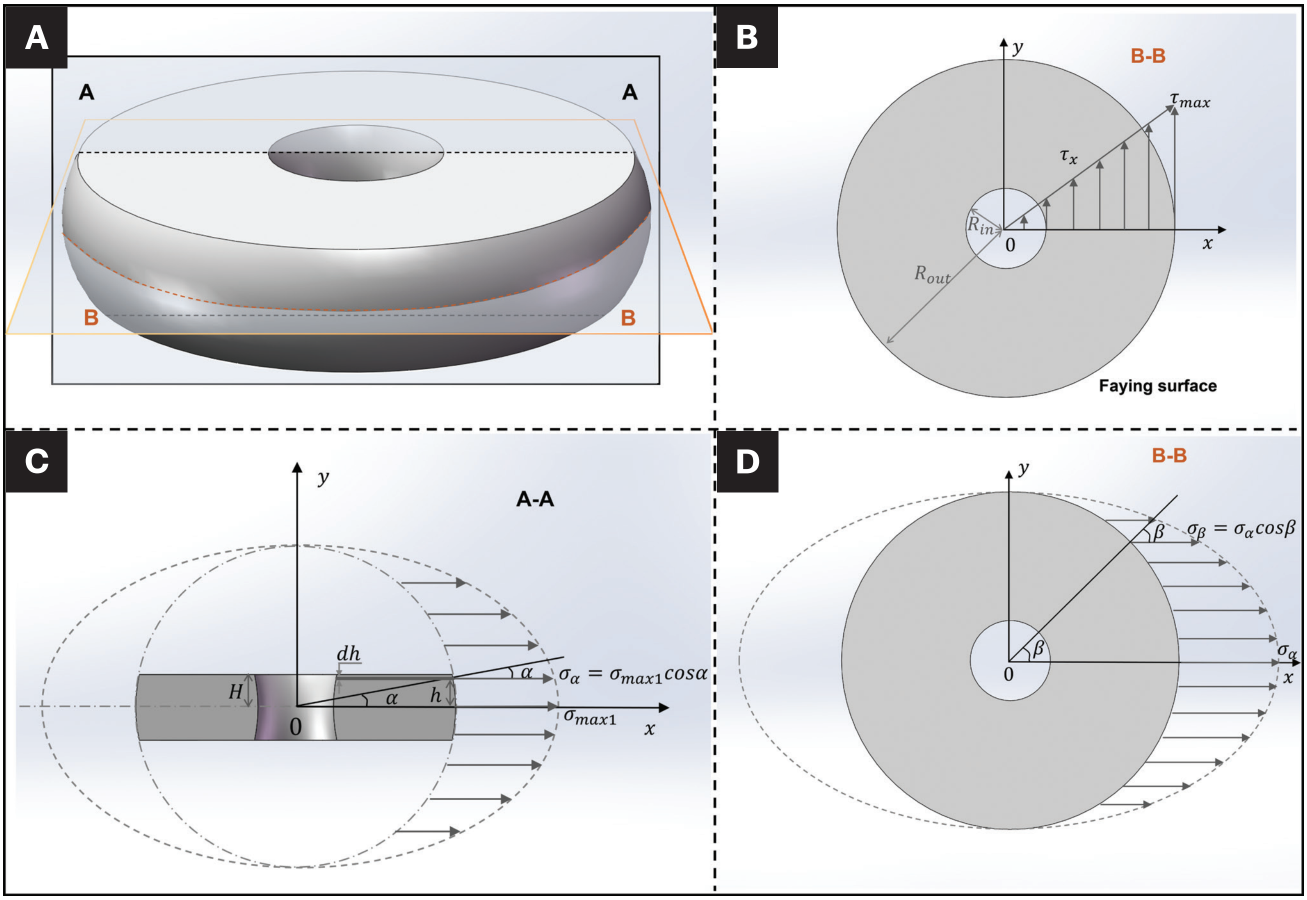

Fig. 12 — Distribution of shear stress in the annular-nugget under tensile-shear load: A — Idealized model of the annular nugget; B — shear stress distribution at the faying surface; C — the detailed tensile stress distribution on the outer side of the nugget; D — tensile stress distribution state at the circumference of the nugget.

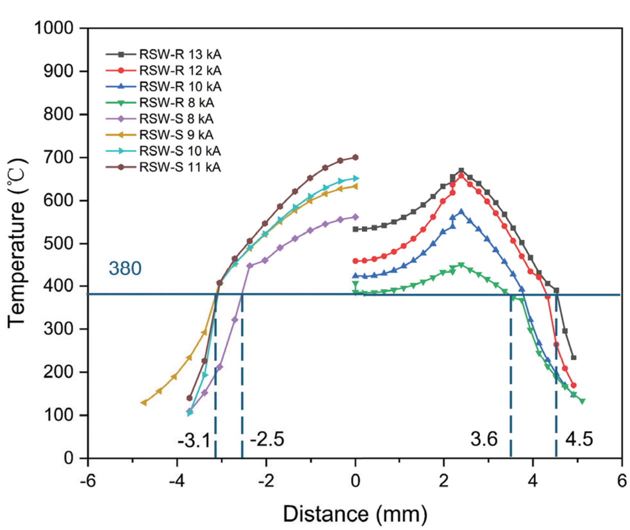

Fig. 13 — Temperature distribution curves along the path on electrode surfaces under two electrode conditions at an energization time of 0.2 s.

is the axial thickness of one side of the annular-nugget, and T is the thickness of the base metal.

σ_α represents the tensile stress at point a on the outside of the horizontal interface of the annular-nugget, cos α is the cosine of the angle between the outside of the annular-nugget at point α and the horizontal interface of the nugget, while cos α is the cosine of the angle between the axial thickness side of the annular-nugget at point α' and the horizontal interface. σ_β represents the tensile stress at any point (α, β) on the outside of the annular-nugget. σ_{HAZ} denotes the ultimate tensile strength of the heat-affected zone, σ_{FZ} represents the ultimate tensile strength of the fusion zone, and σ_{BM} corresponds to the ultimate tensile strength of the base material. V_{HAZ}, V_{FZ}, and V_{BM} are the Vickers hardness values of the heat-affected zone, fusion zone, and base material, respectively. B_1, B_2, and B_3 are the coefficients describing the linear relationship between the ultimate tensile strength and Vickers hardness for each corresponding region.

The h is the vertical height from any point (α, β) on the outside of the annular-nugget to the horizontal interface of the nugget, and cos β is the cosine of the angle between point (α, β) and point α. cos β' is the cosine of the angle between point (α, β) and the point of maximum tensile stress in the horizontal interface of the outer base material along the thickness direction. According to the analysis shown in Fig.

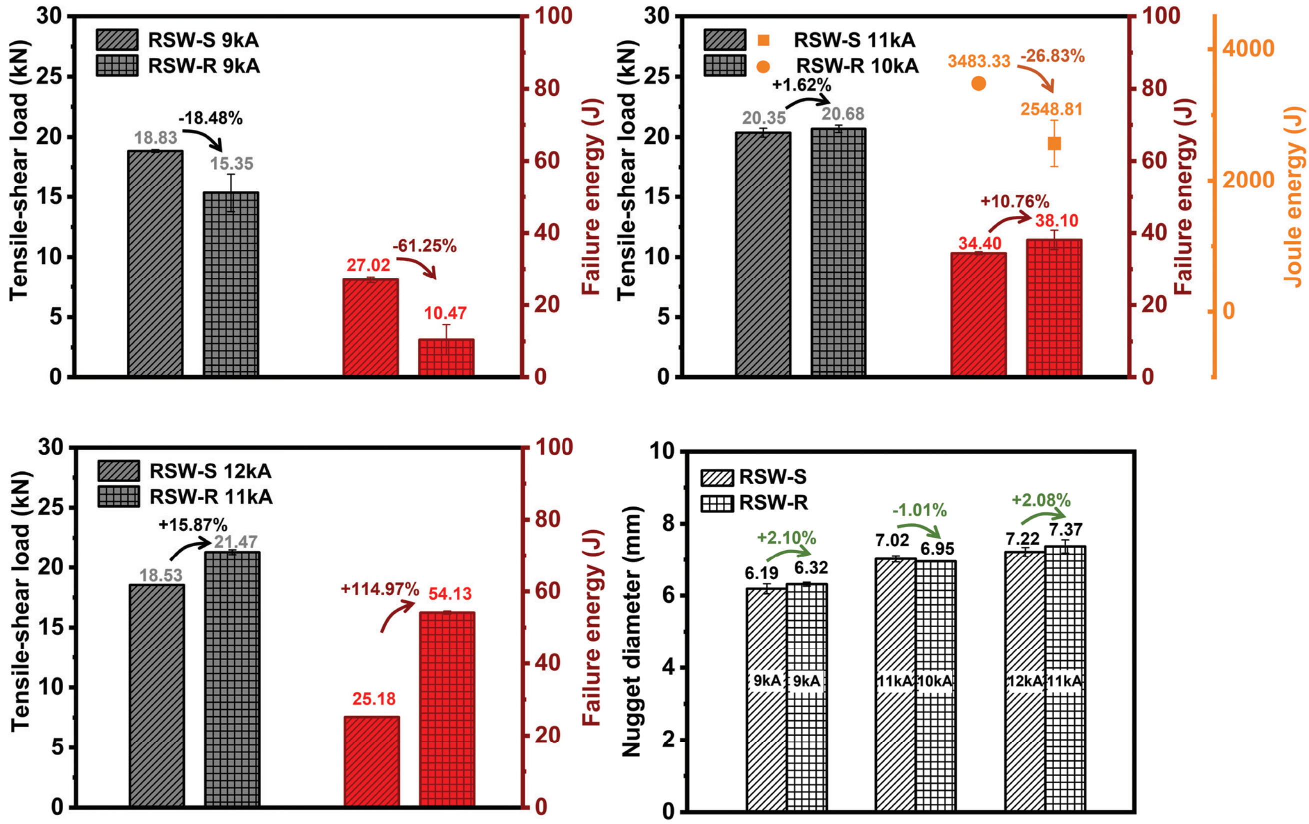

Fig. 14 — Schematic diagram of peak tensile-shear load, failure energy, and joule heat input under RSW-R and RSW-S conditions when the nugget diameter was approximately the same.

10, the primary factors affecting the tensile-shear mechanical properties of the joints varied depending on the failure mode. Building upon previous research, this work optimized the mechanical model and derived a failure mode transition criterion applicable to annular-nugget joints under tensile-shear load. It should be noted that the relationships derived here will be utilized in subsequent sections to deepen the understanding of the strengthening mechanisms associated with annular-nugget joints.

Discussion

Life of RSW-R

As the number of welds increased, progressive changes in electrode tip morphology altered the contact conditions and current distribution at the faying surface, affecting nugget formation. Although tensile-shear load correlated linearly with nugget diameter and area, variations in inner and outer diameters complicated the direct linkage between mechanical performance and electrode life. To better reflect electrode wear, this study evaluated the average nugget dimensions and their relative change rates across successive welding intervals. As shown by the small error bars in Figs. 4A and C, nugget dimensions remained highly stable within each interval.

Under RSW-R conditions, nugget growth behavior diverged from that under RSW-S. Repeated welding caused electrode softening and deformation, increasing the curvature of the RSW-R and expanding the contact area. This promoted outward nugget growth while reducing current density at the faying surface. These competing effects led to a slower increase in outer diameter and a more pronounced inner diameter expansion, thereby reducing the effective nugget volume.

Figure 13 shows the simulated radial temperature distribution on the electrode tip at an energization time of 0.2 s. The spherical electrode exhibited peak temperatures at the tip's center, while the ring conductive electrode's peak occurred along the annular conductive region. In both cases, these high-temperature zones were located above the nugget, where heat dissipation through the electrode was shortest, leading to localized heat accumulation. These regions also coincided with current injection sites, where contact resistance contributed to additional joule heating.

RSW-S presented a sharper peak with a narrower high-temperature zone, while RSW-R displayed a lower peak but a broader high-temperature zone. Elevated peak temperatures accelerated electrode softening. As previously reported (Ref. 22), both the total joule heat input and peak nugget temperature were lower under RSW-R. In contrast, the higher temperatures under RSW-S likely intensified molten metal expansion, increasing the electrode force on the tip.

These combined effects — higher temperature and greater pressure — may have accounted for the larger variation in nugget dimensions observed in the third interval under RSW-S compared to RSW-R. However, in the fourth interval, both electrode types showed a marked increase in nugget variation. Thus, electrode dressing is recommended after approximately 150 consecutive welds for both designs. Importantly, the newly ring conductive electrode did not exhibit a shorter service life than the conventional spherical electrode.

Strengthening Mechanism of Annular-Nugget Joint

As shown in Fig. 5, under identical welding parameters, the peak tensile-shear load and failure energy of annular-nugget joints produced under RSW-R conditions were significantly lower than those of elliptical nugget joints under RSW-S conditions when IF occurred. However, when PF occurred, the peak tensile-shear load and failure energy were higher than those of the elliptical nugget joints. As indicated in Fig. 14, at approximately the same nugget diameter (with a variation within 2.10%), the peak tensile-shear load and failure energy of annular-nugget joints were lower than those of elliptical nugget joints in the case of IF. However, they remained comparable in the case of PF.

When a weld at the nugget connects two sheets, the nugget dimensions primarily determine the load-bearing capacity (Ref. 36). In this study, consistent with the findings of Zhang et al. (Ref. 37), the unconnected region within the annular-nugget (i.e., its inner diameter) had minimal influence on the peak load at higher welding currents but significantly reduced the peak load under lower current conditions.

From Equations 1, 5, and 6, the maximum shear force that the faying surface of the nugget can withstand is influenced by the outer diameter, inner diameter, and hardness of the annular-nugget. Previous studies have shown that the nugget microhardness of DP780 joints remains unaffected by variations in welding electrodes or welding parameters; therefore, for this material, the maximum shear force that the faying surface of the annular-nugget can withstand depends solely on the inner and outer diameters of the nugget under different welding conditions (Ref. 40). A larger outer diameter, smaller inner diameter, and higher hardness collectively contribute to an increased shear force limit. Similarly, as shown in Equations 2, 3, 5, and 6, the maximum tensile force the joint can withstand under tensile-shear loading depends on the fracture zone's hardness and the nugget's outer diameter. The ring conductive electrode reduced joule heat input and peak temperature in the joint, increasing the outer diameter of the annular-nugget while simultaneously delaying hardness degradation in the joint's weak zone (subcritical heat-affected zone). A larger outer diameter and higher hardness in the fracture zone enhance the joint's tensile force limit. At low welding currents, the presence of an internal unconnected region reduced the effective nugget area, thereby lowering the shear force limit and increasing the likelihood of interfacial fracture. Conversely, during pullout fracture, the joint's weak zone area increased with the nugget diameter, increasing the maximum tensile force in this region and ultimately resulting in a higher peak tensile-shear load.

This study found that the unconnected area within the annular-nugget's inner diameter had no adverse effects on the static load-bearing capacity when PF occurred. As demonstrated in Part 1, the annular current distribution in RSW-R reduced the current density at the faying surface, significantly broadening the weldability range of DP780 steel. The shift in nugget growth initiation location and the increase in the upper welding current limit contributed to the enlargement of the nugget diameter. A larger nugget outer diameter enhanced the upper limit of the peak tensile-shear load by approximately 15.9%, thereby improving the strength of the annular-nugget joint. Furthermore, Part 1 also showed that for a similar peak tensile-shear load, RSW-R achieved a 26.83% reduction in joule heat input and an 87.26% reduction in surface indentation compared to RSW-S, further demonstrating its advantages in improving weld quality and mechanical performance.

As shown in Fig. 5, failure energy under RSW-R conditions decreases at high heat inputs, likely due to microstructural evolution caused by varying heat inputs (Ref. 38). The condition of the HAZ also influences the joint's peak tensile-shear load (Ref. 39). In this study, the reduction in failure energy at high heat inputs may be attributed to increased tempering of martensite in the subcritical heat-affected zone of DP780 steel joints, resulting in regional softening (Ref. 40).

Conclusion

This study evaluated the mechanical properties of resistance spot welds produced using the newly developed ring conductive electrode (RSW-R) and the conventional F-type electrode (RSW-S). The investigation identified critical factors influencing the peak tensile-shear load under interfacial fracture and pullout fracture modes and compared the life of two types of electrodes. The findings are summarized as follows:

1. After 150 welds, the variation in the nugget dimensions for both electrodes was approximately 10%. However, after 220 welds, a significant change occurred. The new ring conductive electrode lasted as long as the spherical electrode, with both needing reconditioning after 150 welds.

2. Compared to RSW-S, RSW-R increased the upper limit of peak tensile-shear load by 15.9% and enhanced failure energy by 91.5%.

3. In IF mode, the nugget area was the primary factor affecting the peak tensile-shear load, while in PF mode, the nugget diameter played the dominant role. The unconnected region at the inner diameter did not significantly impair the tensile-shear properties of the joint during PF.

Statements and Declarations

Declaration of Competing Interest

The authors declare that they have no known competing financial interests or personal relationships that could have appeared to influence the work reported in this paper.

Acknowledgment

This work was supported by the Jilin Scientific and Technological Development Program (CN) under Grant (No. 20190302044GX) and supported by the central government-guided local science and technology development fund support projects (Study on Key Technologies of Intelligent Ultrasonic Imaging Detection and Evaluation of Defects in Gas Shielded Welding, 2022L3065).

References

1. Béal, C. T. 2012. Mechanical behaviour of a new automotive high manganese TWIP steel in the presence of liquid zinc. PhD diss. Lyon National Institute of Applied Sciences.

2. Batista, M., and Brandi, S. D. 2013. Use of dynamic resistance and dynamic energy to compare two resistance spot welding equipments for automotive industry in zinc coated and uncoated sheets. *American Journal of Engineering Research* 2(6): 79–93.

3. Bhattacharya, D. 2018. Liquid metal embrittlement during resistance spot welding of Zn-coated high-strength steels. *Materials Science and Technology* 34(15): 1809–1829.

4. Jaber, H. L., Pouranvari, M., Salim, R. K., Hashim, F. A., and Marashi, S. P. H. 2016. Peak load and energy absorption of DP600 advanced steel resistance spot welds. *Ironmaking & Steelmaking* 44(9): 699–706.

5. Pouranvari, M., and Marashi, S. P. H. 2013. Factors affecting mechanical properties of resistance spot welds. *Materials Science and Technology* 26(9): 1137–1144.

6. Ashiri, R., Marashi, S. P. H., and Park, Y. D. 2018. Weld processing and mechanical responses of 1-GPa TRIP steel resistance spot welds. *Welding Journal* 97(5): 157-s to 169-s.

7. Chuko, W., and Gould, J. 2002. Development of appropriate resistance spot welding practice for transformation-hardened steels - A repeatable and effective methodology for producing a temper diagram for different steels is demonstrated. *Welding Journal* 81(1): 1-s to 7-s.

8. Sun, X., Stephens, E. V., and Khaleel, M. A. 2008. Effects of fusion zone size and failure mode on peak load and energy absorption of advanced high strength steel spot welds under lap shear loading conditions. *Engineering Failure Analysis* 15(4): 356–367.

9. Soomro, I. A., Pedapati, S. R., and Awang, M. 2021. Influence of in situ postweld heat treatment on microstructure and failure behavior of dual-phase steel resistance spot weld. *The International Journal of Advanced Manufacturing Technology* 114(11–12): 3739–3750.

10. Soomro, I. A., Pedapati, S. R., and Awang, M. 2021. Optimization of postweld tempering pulse parameters for maximum load bearing and failure energy absorption in dual phase (DP590) steel resistance spot welds. *Materials Science and Engineering A* 803: 140713.

11. Ordoñez, J. H., Ambriz, R. R., García, C., Plascencia, G., and Jaramillo, D. 2019. Overloading effect on the fatigue strength in resistance spot welding joints of a DP980 steel. *International Journal of Fatigue* 121: 163–171.

12. Ren, S., Ma, N., Tsutsumi, S., Watanabe, G., He, H., Cao, C., and Huang, L. 2022. Post-weld cold working for fatigue strength improvement of resistance spot welded joint of advanced high-strength steel. *Journal of Materials Processing Technology* 299: 117346.

13. Li, S., Yang, S., Lu, Q., Luo, H., and Tao, W. 2018. A novel shim-assisted resistance spot welding process to improve weldability of medium-Mn transformation-induced plasticity steel. *Metallurgical and Materials Transactions B* 50(1): 1–9.

14. Li, Y. B., Zhang, Q. X., Qi, L., and David, S. A. 2018. Improving austenitic stainless steel resistance spot weld quality using external magnetic field. *Science and Technology of Welding and Joining* 23(7): 619–627.

15. Pouranvari, M. 2018. Understanding the factors controlling the interfacial failure strength of advanced high-strength steel resistance spot welds: hardness vs. fracture toughness. *Science and Technology of Welding and Joining* 23(6): 520–526.

16. Deng, L., Li, Y. B., Carlson, B. E., and Sigler, D. R. 2018. Effects of electrode surface topography on aluminum resistance spot welding. *Welding Journal* 97(4): 120-s to 132-s.

17. Chen, T., Ling, Z., Wang, M., and Kong, L. 2020. Effect of a slightly concave electrode on resistance spot welding of Q&P1180 steel. *Journal of Materials Processing Technology* 285: 116797.

18. Kim, D., Yu, J., and Rhee, S. 2016. Effect of a conically shaped hollow electrode on advanced high strength steel in three-sheet resistance spot welding. *International Journal of Precision Engineering and Manufacturing* 17: 331.

19. Ren, D., Zhao, D., Li, C., Liu, L., and Zhao, K. 2019. Resistance ceramic-filled annular welding of thin steel sheets. *Journal of Manufacturing Processes* 45: 588–594.

20. Zhao, D., Ren, D., Song, G., Zhao, K., Liu L., and Zhang, Z. 2020. Comparison of mechanical properties and the nugget formation of composite ceramic-centered annular welding and traditional resistance spot welding. *International Journal of Mechanical Sciences* 187: 105933.

21. Ren, D., Zhao, D., Zhao, K., Liu, L., and He, Z. 2019. Resistance ceramic-filled annular welding of DP980 high-strength steel. *Materials & Design* 183: 108118.

22. Wang, S. W., Xu, G. C., Dong, J., Qiu, Y., Fan, Q. Y., Huang, Z. Y., and Gu, X. P. 2025. Study on weldability and mechanical properties of RSW annular-nugget joint. *Welding Journal* 104(6): 175-s to 186-s.

23. AWS D8.9M, 2002, *Recommended Practices for Test Methods for Evaluating the Resistance Spot Welding Behavior of Automotive Sheet Steel Materials*, 79.

24. Pouranvari, M., and Marashi, S. P. H. 2013. Critical review of automotive steels spot welding: process, structure and properties. *Science and Technology of Welding and Joining* 18(5): 361–403.

25. Zhang, Y. Z., Xu, W., Zhang, G. T., Tao, W., and Yang, S. L. 2021. Mechanical behavior and failure mechanism of Q&P980 steel during in situ post-weld heat treatment (PWHT) resistance spot welding. *Metallurgical and Materials Transactions A* 53 (3): 794–809.

26. Mahmud, K., Murugan, S. P., Cho, Y., Ji, C., Nam, D., and Park, Y. D. 2021. Geometrical degradation of electrode and liquid metal embrittlement cracking in resistance spot welding. *Journal of Manufacturing Processes* 61: 334–348.

27. Sawhill, J. M., Watanabe, H., and Mitchell, J. W. 1977. Spot weldability of Mn-Mo-Nb, V-N and SAE 1008 steels. *Welding Journal* 56(7): 217-s to 244-s.

28. Barsoum I. 2006. Ductile failure and rupture mechanisms in combined tension and shear. Hållfasthetslara.

29. Marya, M., Wang, K., Hector, L. G., and Gayden, X. 2006. Tensile-shear forces and fracture modes in single and multiple weld specimens in dual-phase steels. *Journal of Manufacturing Science and Engineering* 128(1): 287–298.

30. Sun, X., Stephens, E. V., Davies, R. W., Khaleel, M. A., and Spinella, D. J. 2004. Effects of fusion zone size on failure modes and

static strength of aluminum resistance spot welds. *Welding Journal* 83(11): 308-s to 318-s.

31. Pouranvari, M., and Marashi, S. P. H. 2011. Failure mode transition in AHSS resistance spot welds. Part I. Controlling factors. *Materials Science and Engineering A* 528: 8337–8343.

32. Pouranvari, M., Asgari, H. R., Mosavizadeh, S. M., Marashi, P. H., and Goodarzi, M. 2007. Effect of weld nugget size on overload failure mode of resistance spot welds. *Science and Technology of Welding and Joining* 12(3): 217–225.

33. Chao, Y. J. 2003. Ultimate strength and failure mechanism of resistance spot weld subjected to tensile, shear, or combined tensile/shear loads. *Journal of Engineering Materials and Technology* 125(2): 125–132.

34. Deng, X., Chen, W., and Shi, G. 2000. Three-dimensional finite element analysis of the mechanical behavior of spot welds. *Finite Elements in Analysis and Design* 35(1): 17–39.

35. Chuko, W. L., and Gould, J. E. 2002. Development of appropriate resistance spot welding practice for transformation-hardened steels. *Welding Journal* 81(1): 1-s to 7-s.

36. Zhang, H., and Senkara, J. 2011. Resistance welding: Fundamentals and applications. Leiden, Netherlands: CRC Press.

37. Zhang, H., Zhou, M., and Hu, S. J. 2001. Impact strength measurement of spot welds. *Proceedings of the Institution of Mechanical Engineers, Part B* 215(3): 403–414.

38. Shojaee, M., Midawi, A. R. H., Barber, B., Ghassemi-Armaki, H., Worswick, M., and Biro, E. 2021. Mechanical properties and failure behavior of resistance spot welded third-generation advanced high strength steels. *Journal of Manufacturing Processes* 65: 364–372.

39. Zhou, M., Zhang, H., and Hu, S. J. 2003. Relationships between quality and attributes of spot welds. *Welding Journal* 4: 72-s to 77-s.

40. Wang, S. W., Xu, G. C., Dong, J., Qiu, Y., Wang, H. X., Wang, C. S., and Gu, X. P. 2025. Study of mechanical properties and failure behavior of DP780 steel RSW under ring conductive electrode. *Engineering Failure Analysis* 170: 109307.

SHENGWEI WANG, **GUOCHENG XU**, **JUAN DONG**, **YU QIU**, and **XIAOPENG GU** (*guxp@jlu.edu.cn*) are with the Key Laboratory of Automobile Materials of Ministry of Education, School of Materials Science and Engineering, Jilin University, Changchun, China. **QIUYUE FAN** is with the Fujian Provincial Key Laboratory of Welding Quality Intelligent Evaluation, Longyan University, Longyan, China. **ZHIYI HUANG** is with the CRRC Changchun Rail Transit Co., Ltd., Changchun, China.